Superconducting theory of confined electrons

Xiuqing Huang [1,2]*
[1]*Department of Telecommunications Engineering ICE, Army Engineering University, Nanjing 210007, China*
[2]*National Laboratory of Solid State Microstructures, Nanjing University, Nanjing, 210093, China*
(Dated: October 20, 2023)

Based on the experimental facts of angle-resolved photoemission spectroscopy (ARPES) and neutron scattering in high-temperature superconductors, a unified theoretical framework centered around polyhedron quantum-well-confined electrons is presented for superconductivity. According to the crystal structure of superconducting materials, the new theory can analytically determine the fundamental properties in copper- and iron-based superconductors, including the Fermi surface structure, the superconducting energy-gap symmetry and value, the superconducting transition temperature, and the spin resonance peaks and parity, the predictions of the theory are in good agreement with experiments. Furthermore, our research provides new insights into the microscopic nature of magnetism, spin, and the Ginzburg-Landau order parameter.

PACS numbers: 74.20. -z, 74.25.Ha, 75.10. -b

I. INTRODUCTION

The discovery of superconductivity by Onnes in 1911 marked a significant milestone in physics [1]. Decades later, the BCS theory explained superconductivity as the result of electron pairing, known as Cooper pairs, through electron-phonon interactions [2]. The advent of copper-based [3–6] and iron-based [7–9] high-temperature superconductors (HTS) greatly challenged existing theories and spurred intense investigations into these materials' unique properties and mechanisms. Microscopic theories and models, including RVB [10], Hubbard models [11], gauge theory [12], spin singlet [13], and d-wave pairing [14], have been proposed, but none of them are considered to be satisfactory.

Angle-resolved photoemission spectroscopy (ARPES) [15] and neutron scattering techniques [16] have emerged as powerful tools for investigating materials' electronic and magnetic properties. By studying the photoemission spectra, one can intuitively obtain visual information about the electronic band structure, Fermi surface topology, and energy gaps related to electronic properties in HTS. Neutron scattering spectra allow researchers to study spin configurations, magnetic excitations, and spin dynamics in the system under investigation, providing information related to magnetism. However, it is unconventional that despite extensive and intensive research efforts, the microscopic mechanism of HTS still needs to be better understood [17].

Angle-resolved photoelectron spectrometers can be likened to a camera because they capture and record information. Experimental results have shown that different superconducting materials exhibit distinct characteristic energy spectrum structures that can reflect even subtle changes in carrier concentration. However, the band theory is built upon the foundation of the Drude quasi-free electron model, where any valence electron can appear anywhere within the superconductor. If this assumption were valid, obtaining a clearly defined Fermi surface structure through experiments would be impossible. A reasonable assumption is that, due to the strong interaction of the lattice Coulomb field, each electron is effectively trapped and confined within a unit cell.

Neutron scattering provides important information about superconductors, such as the magnetic ordering, spin correlations, and spin fluctuations, by utilizing magnetic interactions. On the other hand, superconducting materials exhibit zero resistance in an electric field and demonstrate the Meissner effect in the presence of a magnetic field. Both phenomena are related to the magnetic field as described by Ampere's law. How to interpret and utilize these experimental observations to establish a correct superconductivity theory involves a fundamental yet unresolved question: What is the nature of magnetism?

In this paper, we utilize the reported ARPES and neutron scattering experimental results of copper-based and iron-based superconductors to elucidate the need for new paradigms in the study of superconducting mechanisms. Our findings provide valuable insights into the unique behavior of these materials and successfully develop a unified theory that can explain both conventional and unconventional superconductivity phenomena.

II. CUPRATE SUPERCONDUCTORS

The discovery of cuprate superconductors suggested that superconductivity could occur at temperatures much higher than the BCS theory predicted. It highlighted the need for a more comprehensive theory of superconductivity that can encompass the unique properties exhibited by these materials. However, despite extensive research, a complete and universally accepted theory that explains all aspects of HTS still needs to be developed. The basis of establishing a correct theory lies in experimental facts. So, what insights do experiments provide?

* xiuqing_huang@163.com

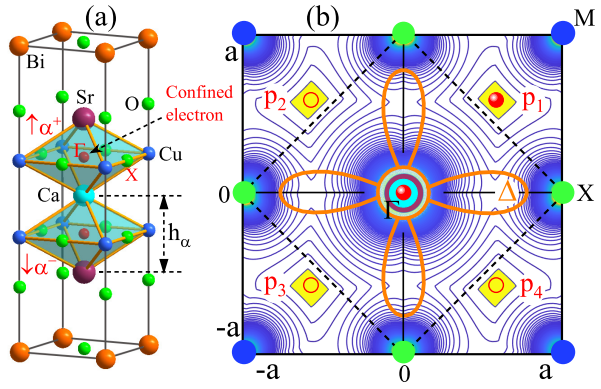

FIG. 1. (a) Octahedral cages (quantum well) and localized electrons in cuprate Bi-2212, (b) Fermi pocket and d-wave symmetry in a unit cell of CuO_2 plane.

A. Octahedral quantum confinement and T_c

Since the high-quality $Bi_2Sr_2CaCu_2O_{8+\delta}$ (Bi-2212) single crystal samples within a relatively wide range of doping levels can be prepared at the laboratory level and it is easy to cleave to get smooth sample surface for ARPES measurements, the Bi-2212 superconductor has been intense studied by ARPES [18]. It is generally believed that the CuO_2 plane plays a fundamental role in cuprate superconductors. The movement of charge carriers (electrons) within the CuO_2 plane leads to the formation of Cooper pairs responsible for the superconducting state. This assumption does not conform to the actual situation in the CuO_2 plane. As shown in Fig. 1(a), the strong Coulomb interactions between the surrounding lattice ions inevitably confine the electrons within a quantum well shaped like an octahedron. Obviously, without the influence of an external field, these electrons are trapped inside the wells and cannot escape to become free electrons.

Figure 1(b) presents a numerical simulation of the electromagnetic force exerted by confined electrons on the CuO_2 surface within the octahedron. Two types of electrons can exist: the central Γ-electrons and the p-electrons located in the four yellow pockets. The material's superconducting properties are determined by the ground state Γ-electrons, which experience the strongest Coulomb confinement inside the center of the octahedron. The excited state p-electrons, with weaker constraints, can easily escape the confinement of the octahedron and become photoelectrons when they acquire photon energy. In ARPES experiments [19, 20], these photoelectrons accumulate over time to form Fermi arcs or Fermi pockets. When $T < T_c$, the p-electrons can return to the ground state and become superconducting Γ-electrons. However, when $T > T_c$, under the Coulomb attraction of the copper ions (M), the Γ-electrons transition to the excited state in the diagonal direction (nodal) as p-electrons, while in the horizontal and vertical directions (X), they form large energy gaps due to the Coulomb repulsion of oxygen ions. Therefore, the pseudogap and d-wave symmetry result from electromagnetic interactions between localized electrons within a single unit cell of the CuO_2 plane and have no direct relationship with the superconducting mechanism.

TABLE I. The relationship between T_c of copper-based superconductors and the distance h between two vertices of octahedral quantum well, $h = h_\alpha$ (or h_β), where $\lambda = T_c h^2$. The values in bold are possible superconducting phases.

Compound	T_c (K)	h_α (Å)	h_β (Å)	λ
$YBa_2Cu_3O_{7-\delta}$	93	**3.6720**		1254
$Bi_2Sr_2Ca_2Cu_3O_{10+\delta}$	110	3.1511	**3.3272**	1217
$TlBa_2CaCu_2O_{7+\delta}$	103	**3.5771**		1317
$TlBa_2Ca_3Cu_4O_{11+\delta}$	112	3.2453	**3.5025**	1373
$TlBa_2Ca_2Cu_3O_{10+\delta}$	120	**3.2381**	3.5305	1258
$Tl_2Ba_2Ca_2Cu_3O_{10+\delta}$	128	**3.3053**	3.5252	1393
$HgBa_2CuO_{4+\delta}$	94	**3.8241**		1374
$HgBa_2Ca_2Cu_3O_{8+\delta}$	134	**3.2108**	3.4241	1380

As shown in Fig. 1(a), Bi-2212 exhibits two degenerate octahedra with corresponding electron states of opposite orientations. We can use the distance h_α between the two vertices of the octahedron to characterize the degree of electron confinement. The smaller the h_α value, the stronger the electron confinement and the stronger the association between the Γ-electron and the octahedron. Consequently, the superconducting gap increases, and the superconducting transition temperature increases. The data in Table 1 can easily verify this conclusion. The table shows that there are usually two sets of different octahedra in copper-based superconductors, corresponding to the α and β superconducting phases. Under applied pressure, the low-temperature superconducting β phase with big h_β will transition to the high-temperature superconducting α phase with small h_α. This issue will be discussed in detail later. Based on the statistical data in Table I, the relationship between the superconducting gap Δ, the superconducting transition temperature T_c, and $h = h_{\alpha(\beta)}$ is as follows:

$$\triangle \propto T_c = \frac{\overline{\lambda}}{h^2} \simeq \frac{1320}{h^2}. \quad (1)$$

It is necessary to emphasize that the commonly accepted academic viewpoint that better conductivity leads to easier achievement of superconductivity needs to be corrected. Conductivity and superconductivity are usually contradictory to each other. As is well-known, the best conductors, like gold, silver, and copper, are not superconductors; conversely, high-temperature superconductors usually originate from insulators. The essence of the pressure effect is to increase electron localization, which confirms that stronger electron localization is more likely to achieve higher-temperature superconductivity.

B. Bilayer-split Fermi surface Sheets in Bi-2212

Figs. 1(a) shows that a pair of twinned octahedra connected by calcium (Ca) can be constructed in the Bi-2212 unit cell, with each octahedron corresponding to a set of Fermi surface sheets (Fermi arcs). Under low doping conditions, the

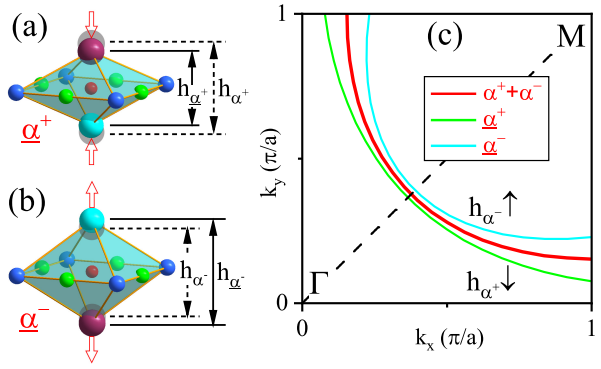

FIG. 2. Fermi surface bilayer-splitting induced by Jahn-Teller effect in Bi2212. (a) the octahedron-confined electronic state of antibonding contraction, (b) the bonding octahedron electronic state, and (c) the double splitting of the red degenerate Fermi arc.

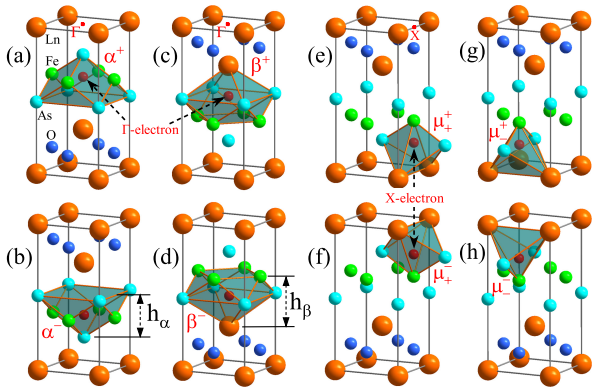

FIG. 3. Confined electrons in the iron-based 1111 superconductor. (a) and (b) The nonahedron confinement cages (quantum-well); (c) and (d) the tri-decahedron confinement cages; (e) - (h) the tetrahedron confinement cages.

octahedra do not undergo distortion, and $h_\alpha = h_{\alpha^+} = h_{\alpha^-}$, as shown by the dotted line in Figs. 2(a) and (b). Hence, in ARPES experiments, a doubly degenerate Fermi arc indicated by the red line in Fig. 2(c) can be observed. In the case of over-doping, an uneven distribution of dopants can occur in the upper and lower octahedra. Assuming that the upper octahedron has a higher doping level than the lower one, the Sr and Ca ions at the vertices contract inward under the Coulomb attraction of the doped electrons, leading to the occurrence of the Jahn-Teller effect and causing distortion of the octahedra. The heavily doped octahedron h_{α^+} compresses to $h_{\underline{\alpha}^+}$ (antibonding), while the weakly doped octahedron h_{α^-} stretches to $h_{\underline{\alpha}^-}$ (bonding), as shown by the solid line in Figs. 2(a) and (b). As a result, the originally degenerate red Fermi arc splits into two separate Fermi arcs with different energy gaps, represented by the green and cyan lines, as shown in Fig. 2(c).

According to Eq. (1), the superconductivity corresponding to the antibonding $\underline{\alpha}^+$ phase has a larger superconductivity energy gap than that corresponding to bonding $\underline{\alpha}^-$ phase. Due to the antibonding contraction of the octahedron in Fig. 2 (a), Sr and Ca ions have stronger Coulomb attraction to p-electrons inside the pockets along the direction Γ, and the red Fermi arc in Fig. 2(c) will shift along the direction Γ to form a green non-degenerate large Fermi arc. In the binding case of Fig. 2(b), the octahedra expands, reducing the p-electrons' binding. Under the attraction of copper ions at the M site, the p-electrons bend towards the M direction, forming a small cyan Fermi arc as shown in Fig. 2(c). Surprisingly, the theoretical analysis based on the localized electrons in the octahedra is in complete agreement with the high-resolution laser-ARPES measurements [21].

III. IRON-BASED SUPERCONDUCTORS

As a second class of HTS, iron-based superconductors have a lower critical temperature compared to copper-based superconductors. However, due to their extensive family of compounds, they provide a much richer variety of experimental samples and data for the study of high-temperature superconductivity mechanisms. Understanding the similarities and differences between these two classes of superconductors is essential for developing a comprehensive theory of high-temperature superconductivity.

A. Quantum confinement and T_c

The discovery of iron-based superconductors has generated significant interest in the scientific community due to their unique properties [22]. The 1111 series represents the first family of iron-based superconductors discovered and currently boasts the highest superconducting transition temperatures. This series can be denoted as LnFeAsO, where Ln represents elements such as La, Sm, Ce, Nd, Gd, and F commonly substitutes the O position. The FeAs layer is a crucial structural component in iron-based superconductors, and the superconducting behavior is closely associated with these FeAs layers. Copper-based superconductors exhibit a two-dimensional CuO_2 layer structure, whereas iron-based superconductors possess a folded layer structure of As-Fe-As. This structural disparity influences the electronic behavior and properties of these superconductors. Copper-based superconductors exhibit an anisotropic d-wave symmetry in their superconducting energy gap. In contrast, iron-based superconductors display more complex energy gap symmetries, including s-wave, d-wave, and (s±)-wave, depending on the specific material and its doping level [23, 24].

Unlike the 2D CuO_2 superconducting planes in copper-based superconductors, the FeAs layer has a sandwich structure of the As–Fe–As trilayer. According to the electron confinement mechanism proposed in this article, the electron confinement effect of FeAs is undoubtedly weaker than that of the CuO_2 layer. Qualitatively, it can be predicted that the T_c of iron-based superconductors would be lower than copper-based superconductors.

Figure 3 shows the eight localized electronic states of three

TABLE II. The relationship between T_c of iron-based superconductors and and the height h of polyhedral quantum well, $h = h_\alpha$ (or h_β,h_γ), where $\lambda = T_c h^2$. The values in bold are possible superconducting phases.

Compound	T_c(K)	h_α (Å)	h_β (Å)	h_γ (Å)	λ
$LaFeAsO_{1-x}F_x$	43	2.6723	**3.0749**		406
$SmFeAsO_{1-x}F_x$	43	2.7291	**3.0792**		407
$SmFeAsO_{1-x}F_x$	55	**2.7149**	3.0433		405
$TbFeAsO_{1-x}F_x$	45	2.7567	**3.0501**		418
$GdFeAsO_{1-x}F_x$	53.5	**2.7454**	3.0568		403
$PrFeAsO_{1-x}F_x$	52	**2.6857**	3.0591		375
$NdFeAsO_{1-x}F_x$	50	**2.7227**	3.0418		371
$CeFeAsO_{1-x}F_x$	41	2.6930	**3.0777**		388
$LaFeAsO$	41	2.6608	**3.0912**		392
$LaYFeAsO$	42	2.6840	**3.0912**		401
$BaKFe_2As_2$	38	2.7650	**3.3242**		419
$CaKFe_4As_4$	35	2.5617	2.9276	**3.3874**	402
$KCa_2Fe_4As_4F_2$	33	2.8406	3.0301	**3.4353**	390

possible types in the 1111 superconductor. Figs. 3(a) and (b) are the $\alpha^{\pm}$ phase of the nonahedron, Figs. 3(c) and (d) are the $\beta^{\pm}$ phase of the tri-decahedron, and Figs. 3(e) - (h) are the $\mu^{\pm}_{\pm}$ phase of the tetrahedron. The $\alpha^{\pm}$ and $\beta^{\pm}$ phases correspond to two pairs of degenerate states, where the electrons are localized respectively in the center of iron and arsenic layer cells; these four kinds of electrons contribute to the superconductivity. Each polyhedron represents a superconducting phase, and the height of the polyhedron determines the superconducting gap and the superconducting transition temperature. Since h_α is smaller than h_β, the $\alpha^{\pm}$ phase has a higher T_c than the $\beta^{\pm}$ phase. In the case of the tetrahedron, the $\mu^{\pm}_{\pm}$ phase restricts the X-electrons, which do not determine the superconducting gap or transition temperature. The restriction on electrons of $\mu^{\pm}_{\pm}$ is the weakest, resulting in the most minor binding energy between the electron and the tetrahedron and corresponding to the smallest Fermi surface structure.

Similar to copper-based superconductors. Table II shows the relationship between the superconducting transition temperature and the height of the Γ-electron polyhedra in iron-based superconductors. It can be observed that the majority of iron-based superconductors exhibit a dual-phase behavior, while a few can exhibit a triple-phase behavior. These findings can be verified through neutron spin resonance and pressure experiments, which will be discussed in detail later in the paper. Similarly, the relationship between the superconducting gap Δ, T_c, and $h = h_{\alpha(\beta,\gamma)}$ can be obtained as

$$\triangle \propto T_c = \frac{\overline{\lambda}}{h^2} \simeq \frac{400}{h^2}. \quad (2)$$

The value $\overline{\lambda}$ determines the strength of the restriction on superconducting Γ-electrons in superconducting materials. A larger $\overline{\lambda}$ implies stronger electron localization and a higher T_c. Comparing Eq. (1) and Eq. (2), the value of $\overline{\lambda}$ for copper-based superconductors is approximately three times

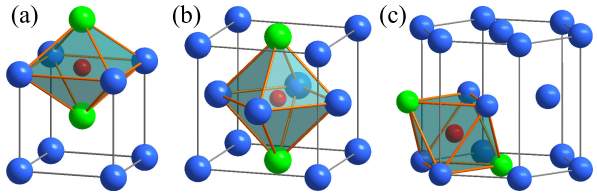

FIG. 4. The octahedral confinement of superconducting electrons in conventional elemental superconductors. (a) BCC, (b) CCP, and (c) HCP.

that of iron-based superconductors. It is known that copper-based superconductors achieved a record T_c of up to 164 K [25] under high pressure, while the record for iron-based superconductors is around 55 K [9]. It is also surprising that the relationship between the two highest superconducting transition temperatures is just three times.

B. D-wave, S-wave or S(+-)-wave?

So far, whether it is copper-based or iron-based superconductors and whether it is theoretical or experimental research, the most critical question for superconductivity researchers is how electrons are paired. Because they firmly believe that the symmetry of the gap function is the key to unraveling the superconducting mechanism. This article presents an entirely different viewpoint on this matter. As shown in Fig. 1(b), the so-called d-wave symmetry is merely the result of the localized electrons within the octahedron interacting with the nearest oxygen ions (negative charges) and the next-nearest copper ions (positive charges) in the CuO_2 plane. In our opinion, the superconducting mechanism needs a new paradigm.

Generally, the energy gap in conventional superconductors is believed to possess typical s-wave symmetry. Figure 4 illustrates three typical crystal structures of elemental superconductors, whether it is body-centered cubic (BCC), face-centered cubic (CCP), or hexagonal close-packed (HCP). The octahedral cage can also describe confined superconducting electrons. Due to the crystal's symmetry, it is possible to construct six octahedra with different orientations around the same localized electron, implying that the confined superconducting electrons are isotropic and exhibit a six-fold degeneracy. Consequently, the symmetry of their superconducting energy gap can be approximated as an isotropic s-wave without the presence of nodes observed in quasi-2D copper-based superconductors.

The gap symmetry in iron-based superconductors has been a subject of debate. The most commonly observed gap symmetry in iron-based superconductors is an s±-wave symmetry. However, other gap symmetries, such as d-wave and s-wave, have also been proposed and reported. Figure 5(a) shows the crystal structure of $Ba_{1-x}K_xFe_2As_2$ (BKFA) from the 122 family with T_c =38 K, which has been extensively studied using ARPES due to its excellent crystal quality [23].

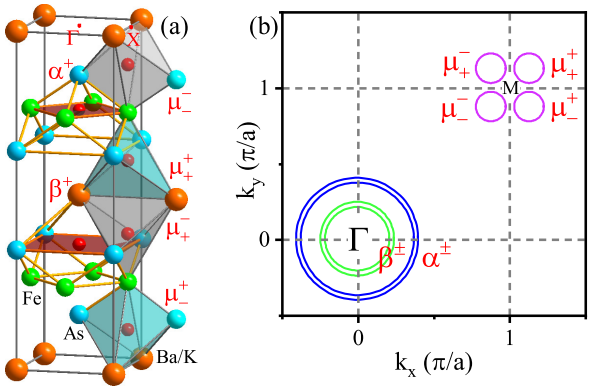

FIG. 5. Confined electrons and corresponding Fermi surfaces in an iron-based 122 superconductor. (a) Three kinds of eight localized electrons inside 122; (b) the corresponding eight fermi surface.

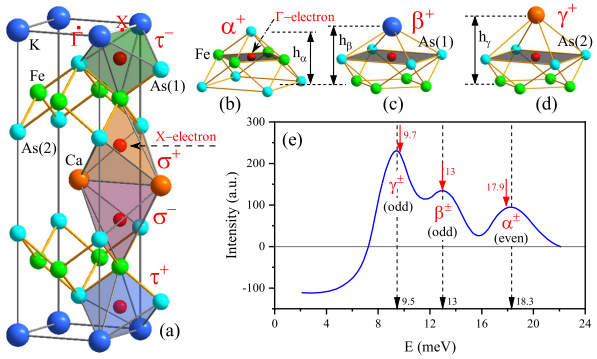

FIG. 6. Neutron spin resonance mode and mode symmetry of 1144 iron-based superconductors. (a) The crystal structure of $CaKFe_4As_4$, (b)-(d) three localized phases of $\Gamma-$electrons and corresponding confined polyhedrons, and (e) neutron spin resonance peaks and odd-even symmetry corresponding to three confined electrons.

The BKFA of Fig. 5(a) also exhibits two types of doubly degenerate superconducting electronic states, denoted as $\alpha^{\pm}$ and $\beta^{\pm}$. The 38 K phase corresponds to the low-T_c $\beta^{\pm}$ phase, while the high-T_c $\alpha^{\pm}$ phase can be predicted with approximately 52 K based on the structural data in Table II. The phase transition from the low-T_c $\beta^{\pm}$ phase to the high-T_c $\alpha^{\pm}$ phase is possible by pressure. This pressure-induced phase transition has already been achieved in similar superconductors like KFe_2Se_2 [26].

Regarding the size and symmetry of the energy gap, firstly, $h_\alpha < h_\beta$, then it can be concluded that the energy gap of the two superconducting phases satisfies: $\Delta_\alpha > \Delta_\beta$. As for the energy gap symmetry, it must be clear that it comes from the local symmetry of the polyhedral quantum well in Fig. 5(a). Qualitatively, due to the absence of highly symmetric octahedra found in Fig. 4 elemental superconductors and the lack of octahedra containing strict 2D copper-oxygen planes like those in Fig. 1 for copper-based superconductors, therefore, the energy gap symmetry of iron-based superconductor is neither the s-wave of elemental superconductors nor the d-wave of copper-based superconductors, of course, it is not a strict $S^{\pm}$-wave. This issue does not require excessive attention and interpretation as it is not directly related to the superconducting mechanism.

The Fermi surface has always been imbued with a great deal of mystique, but in reality, it is just an image of the electron states in real space. In Fig. 5(a), the eight electron states each contribute to a closed circular ring on the Fermi surface shown in Fig. 5(b). The higher the binding energy between the localized electrons in real space and the polyhedral quantum well, the larger the corresponding radius of the Fermi surface. The $\alpha^{\pm}$ and $\beta^{\pm}$ electrons at the center point Γ of Fig. 5(a) contribute to two concentric large Fermi rings at Γ of Fig. 5(b), while the four electrons at point X contribute to four small rings at point $M(\pi,\pi)$ of Fig. 5(b). As shown in Fig. 5(b), the theoretical Fermi surface obtained based on the localized electrons in real space perfectly matches the experimentally reported results [23, 27].

C. Resonant modes and symmetries in 1144 compound

The crystal structure of the 1144 iron-based superconductor closely resembles that of the 122 series. Research on the 1144 superconductors mainly focuses on $CaKFe_4As_4$ of Fig. 6(a). Comparing Fig. 6 and Fig. 5, two distinctions between the two compounds are apparent. Firstly, the 122 has two $\Gamma-$electron states ($\alpha^{\pm}$ and $\beta^{\pm}$) , while the 1144 system has three $\Gamma-$electron states ($\alpha^{\pm}$,$\beta^{\pm}$ and $\gamma^{\pm}$). This results in observing three double-degenerate Fermi surfaces in high-resolution laser-ARPES experiments on the 1144 series. Secondly, the 122 series has a quadruple degenerate $X-$electron. In comparison, the 1144 series has two doubly degenerate $X-$electrons, which leads to their slightly different Fermi surface at point M. From the confined polyhedron structure and quantity, 1144 shows greater similarity with 12442 of $KCa_2Fe_4As_4F_2$ superconductor, leading to almost the same Fermi surface structure [28].

This section focuses on the experimental results of inelastic neutron scattering conducted by Xie et al. on $CaKFe_4As_4$ [29]. We explain the origins of the observed triplet spin resonance modes and odd-even symmetries. Here, the resonance modes observed in the neutron scattering experiment are believed to arise from the contribution of $\Gamma-$electrons. In Fig. 6, it can be observed that $CaKFe_4As_4$ possesses three types of $\Gamma-$electrons, which are the nonahedron $\alpha^{\pm}$ electron of Fig. 6(b), the tri-decahedron $\beta^{\pm}$ electron of Fig. 6(c) and the tri-decahedron electron $\gamma^{\pm}$ of Fig. 6(d). Each type of electron contributes to one definite spin resonance mode; hence, triplet spin resonance modes exist in the experiment. The resonance energy is directly proportional to the superconducting energy gap, as per Eq. (2), which establishes a relationship between the resonance energy and the height of the polyhedron of Figs. 6(b)-(d) as follows.

$$E_R = \frac{\Theta}{h_i^2},\ i = \alpha, \beta, \gamma, \tag{3}$$

where Θ is the undetermined coefficient.

According to the crystal structure data of Ref.[29], $c = 12.63$ Å and $zc = 5.855$ Å (the distance between adjacent Fe-Fe planes), resulting in $h_\alpha = 2.504$ Å, $h_\beta = zc/2 = 2.928$ Å, and $h_\gamma = (1-z)c/2 = 3.387$ Å. As shown in Fig. 6(e), assuming the resonance peak $E_R(\beta)$ of phase $\beta^\pm$ is 13 meV, by applying Eq. (3) we can determine the resonance peaks of phase $\alpha^\pm$ and phase $\gamma^\pm$ as $E_R(\alpha) = 17.9$ meV and $E_R(\gamma) = 9.7$ meV, which are consistent with the experimental values of 18.3 meV and 9.5 meV, respectively. In their experiments [29], they observed that the spin resonance mode of the 1144 superconductor exhibits two modulation modes: odd mode and even mode. We believe this difference also comes from the nature of polyhedron. It can be seen from Fig. 6 that the $\alpha^\pm$ electrons are confined in the Fe layer, corresponding to even symmetry, while $\beta^\pm$ and $\gamma^\pm$ electrons are confined in the As(1) and As(2) layers, respectively, corresponding to odd symmetry. The polyhedron structure determines this odd-even modulation of the spin resonance mode and cannot be used as evidence of superconducting pairing.

D. Fermi surface of single-layer FeSe superconductor

Due to their remarkable properties and potential applications, single-layer iron-based superconductors have garnered considerable interest. These materials comprise a solitary layer of iron atoms nestled between two layers of chalcogenide atoms. One particularly intriguing aspect of single-layer FeSe is its distinct Fermi surface, setting it apart from other iron-based superconductors (refer to Fig. 5(b)). The Fermi surface of FeSe consists of pockets near the zone corner, devoid of any indication of a Fermi surface around the zone center [30]. The underlying reason for this distinctive Fermi surface structure remains a mystery.

In the single-layer FeSe superconductor, only the local electronic state of phase α^+ in Fig. 7(a) exists, and the electrons are entirely confined in the central Fe layer. According to Table II, the highest superconducting transition temperature of iron-based superconductor α^+ phase is about 55 K, which is entirely consistent with the conclusion by analyzing the temperature dependence of the superconducting gap [30]. Fig. 7(b) depicts a top view of a single-layer FeSe superconductor with localized electrons, while Fig. 7(c) shows the corresponding Fermi surface. Because there are no localized electrons at point Γ in Fig. 7(b), it is observed that the central area of the Fermi surface in Fig. 7(c) does not exist, but the Fermi surface appears at four corners.

E. Pressure-induced superconducting phase transition

Pressure significantly influences the behavior of superconductors by inducing structural changes that can modify their electronic properties and impact superconductivity. In 2012, Sun et al. studied the effect of pressure on iron-based superconductors, particularly

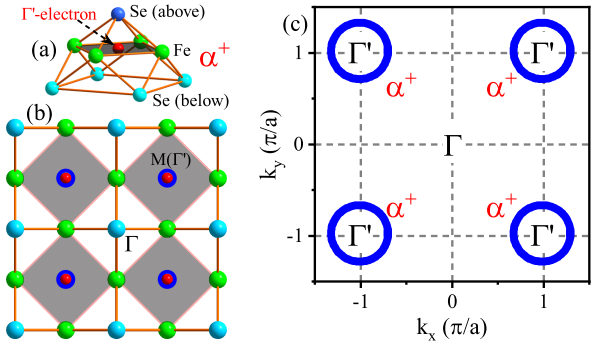

FIG. 7. The Fermi surface mapping of monolayer FeSe superconductor. (a) Localized electrons confined by the nonahedron quantum well, (b) the top view structure of FeSe superconductor, (c) the Fermi surface corresponding to (a).

$K_{0.8}Fe_ySe_2$ [26]. Surprisingly, they observed a second phase transition in superconductivity triggered by pressure. This discovery revealed the coexistence of two distinct superconducting phases within the same material, each characterized by different transition temperatures. This finding challenges existing theories on superconductivity, suggesting the need for a new framework to explain the presence of multiple superconducting phases and their respective transition temperatures. The discovery emphasizes the importance of further exploration and a deeper understanding of superconductivity, which may pave the way for developing innovative superconducting theories.

Next, we will show that the mechanism of pressure-increasing superconducting transition temperature can be well understood within the framework of confined electrons. In this paper, Eq. (2) provides insights into the direct influence of pressure on the height of polyhedral quantum wells in iron-based superconductors. With the application of pressure, the height of the quantum well decreases, which leads to a decrease in the mobility of confined electrons. This reduced mobility can enhance the localization of electrons, potentially leading to a higher T_c superconducting phase.

As shown in Figs. 8(a) and (b), in $K_{0.8}Fe_ySe_2$ superconductors, two types of polyhedron quantum wells can be constructed, each confining localized electrons of type $\alpha^\pm$ and $\beta^\pm$, respectively. These electrons correspond to different superconducting phases: the low-temperature $\beta^\pm$ phase, or the first superconducting phase, represented by Fig. 8(a), and the high-temperature $\alpha^\pm$ phase, or the second superconducting phase, represented by Fig. 8(b). With known values of $h_\alpha = 2.836$ Å and $h_\beta = 3.534$ Å, according to Eq. (2), the highest superconducting transition temperatures for the respective phases can be accurately predicted as 32.1 K for $\beta^\pm$ phase and 49 K for $\alpha^\pm$ phase. These two values closely match the experimentally observed highest transition temperatures, 32K and 48.7 K, for the first and second superconducting phases [26].

In fact, the microscopic electronic behavior of this phase transition process is very simple. In the absence of external pressure, the initial state of electrons in $K_{0.8}Fe_ySe_2$

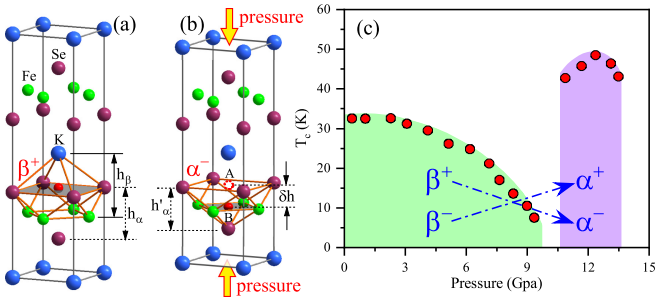

FIG. 8. (a) The low-T_c superconducting β phase in $K_{0.8}Fe_ySe_2$ superconductor without external pressure; (b) the localized electron transfer from A of Se-plane (β^+phase) to B of Fe-plane and the emergence of high-T_c α phase due to pressure; (c) the phase diagram illustrating the phase transition process.

corresponds to the low-temperature superconducting phase $\beta^{\pm}$ with a transition temperature of approximately 32 K, where the electrons are localized in the Se layer. Under external pressure, the lattice undergoes slight distortion, causing the electrons to transfer from the Se layer (A) to the Fe layer (B), as illustrated in Fig. 8(b), with a shift in position δh of approximately 1.4 Å from A to B. As shown in Fig. 8(c), in this process, a phase transition of the superconducting phase occurs ($\beta^+ \rightarrow \alpha^-$, $\beta^- \rightarrow \alpha^+$), where the low-temperature phase $\beta^{\pm}$ above 32 K disappears, and the high-temperature phase $\alpha^{\pm}$ above 49 K emerges.

From the above sections, we show that many vital experiments of copper-based and iron-based superconductors can be well explained only by using the hypothesis of static localized electrons, which is enough to prove that the traditional superconducting theoretical research based on dynamic free electrons is flawed. In the following chapter, we will clarify the physical essence of superconductivity under the new paradigm of confined electrons. Through the research and discussion in this paper, readers can gain a brand-new understanding of the generation of superconducting zero electrical resistance, the Messner effect, the essence of magnetism, the Mott insulator, and the Ginzburg-Landau order parameter.

IV. UNIFIED SUPERCONDUCTING MECHANISM

It is widely recognized that existing theories and models of superconductivity are based on the Drude free electron model, which relies on moving electrons to explain current and magnetic fields. Such a dynamic picture needs continuous external energy to keep the electrons moving endlessly, which contradicts the assumption that superconductivity does not lose energy. Through the above research on copper-based and iron-based superconductor experiments, it is easy to see that superconductivity can be perfectly analyzed in a static localized electron framework, and the physical phase transition can be realized only by a slight displacement of electrons of angstrom level. Based on the above research, next, we propose a unified microscopic mechanism based on Mott insulators with localized electrons, where current and magnetic fields are attributed to Maxwell displacement current and Dirac magnetic monopoles rather than electron motion. Our proposal traces natural magnetic phenomena to the simplest electron-proton pair, where the pairing generates a magnetic field and individual electrons or protons generate an electric field. The proton-electron electric dipole vector is the Ginzburg-Landau order parameter for the superconducting phase transition. [32].

A. What are magnetic monopoles?

The duality between electric and magnetic fields is a fundamental concept in electromagnetism, which implies that generating a magnetic field requires static magnetic charges, as Dirac proposed in the theory of magnetic monopoles. It was suggested that electric and magnetic charges could coexist and satisfy the following quantization condition [33]:

$$eg = \frac{hc}{4\pi}n = \frac{\hbar c}{2}n, \quad n = \pm 1, \pm 2, \pm 3, \cdots \tag{4}$$

where e and g are the electric and magnetic charges, respectively, h is the Plank's constant, and n being the integers.

Using the fine structure constant $\alpha = e^2/4\pi\varepsilon_0\hbar c$, the Eq. (4) can be re-expressed as:

$$g = (\frac{n}{8\pi\varepsilon_0\alpha})e = \Pi_n e, \quad n = \pm 1, \pm 2, \pm 3, \cdots \tag{5}$$

where Π_n is an adjustable constant.

The relationship presented in Eq. (5) above provides a clear understanding that the purported magnetic monopoles are, in fact, just dressed electrons or protons. This means that the superimposed electric field created by the electron-proton pair is the magnetic field. Intriguingly, electrons and protons can

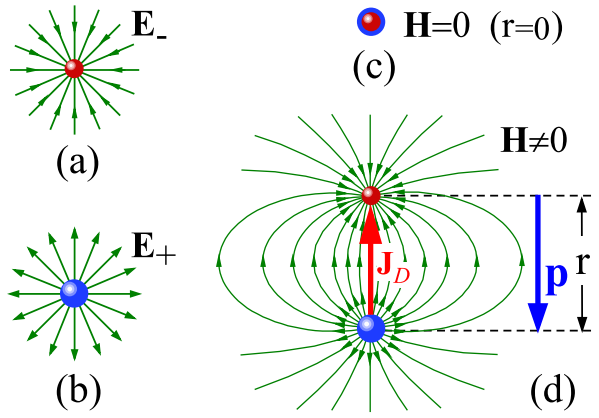

FIG. 9. Relationship between electrostatic field and static magnetic field. (a) and (b) Isolated charges produce electric fields; (c) due to the symmetry ($r = 0$), the electromagnetic field is hidden; (d) when the symmetry is broken ($r \neq 0$), a magnetic field is excited.

simultaneously act as electric and magnetic charges. In the following, we will reconfirm this conclusion in accordance with Maxwell's theory.

Figs. 9(a) and (b) show isolated electron or proton generating electric fields $\mathbf{E}_-$ and $\mathbf{E}_+$ respectively. As in Fig. 9(c), no electromagnetic field exists when coinciding. In Fig. 9(d), a separation of $\mathbf{r}$ forms an electric dipole through symmetry breaking, and a magnetic field emerges. It is well-known that a proton-electron pair can form a hydrogen atom or a neutron, and it is worth emphasizing that the proton-electron pair is the smallest quantized capacitance in nature. According to Maxwell's theory, a displacement current density $\mathbf{J}_D = \varepsilon_0 \partial \mathbf{E}/\partial t$ exists in the capacitor, which will create an associated magnetic field in the surrounding space. As Maxwell's statement suggests, a changing electric field produces a magnetic field, which is given by $\mathbf{H}$ as follows:

$$\mathbf{B} = \mu_0 \mathbf{H} = \frac{\mathbf{E}_+ + \mathbf{E}_-}{c}, \tag{6}$$

where c is the speed of light and μ_0 is the vacuum permeability.

The formula shows that an isolated electron generates only an electric field and lacks spin properties. Modern physics proposes electron spin based on atomic fine spectral structure and Stern-Gerlach silver atomic beam experiment [34]. However, these experiments only show magnetic moments in atoms such as silver or hydrogen (electron-proton pairs), not free electrons.

B. Symmetry of Maxwell's equations

Maxwell's equations are elegant but not invariant under duality transformation. Is the asymmetry between electric and magnetic fields a reflection of nature or our interpretation? We will provide a clear answer. The Maxwell's first equation $\nabla \cdot \mathbf{E} = \rho_e/\varepsilon_0$ and the second equation $\nabla \cdot \mathbf{B} = 0$ are completely independent of each other, so strictly speaking, the electromagnetic field is not unified. Here, we will show that the second equation can be derived from the first. For a proton-electron pair with an electric dipole vector of $\mathbf{p}$, substituting the electric fields excited by the electron and proton into Eq. (6) yields:

$$\nabla \cdot \mathbf{B} = \frac{[\rho_e(\mathbf{r}_p) + \rho_{-e}(\mathbf{r}_p + \mathbf{p}/e)]}{c\varepsilon_0}. \tag{7}$$

Under a far-field approximation $\mathbf{r}_\mathrm{p} >> \mathbf{p}/e$, then $\rho_e(\mathbf{r}_p) + \rho_{-e}(\mathbf{r}_p + \mathbf{p}/e) \simeq 0$, this result means that the right-hand side of the second Maxwell's equation is not exactly zero. Furthermore, our assumption has ruled out the presence of the conduction current ($\mathbf{J}_e = 0$). Thus far, we can now present the corrected Maxwell's equations:

$$\begin{aligned} \nabla \cdot \mathbf{E} &= \frac{\rho_e}{\varepsilon_0}, \\ \nabla \cdot \mathbf{B} &\simeq 0, \\ \nabla \times \mathbf{E} &= -\frac{\partial \mathbf{B}}{\partial t}, \\ \nabla \times \mathbf{B} &= \mu_0 \varepsilon_0 \frac{\partial \mathbf{E}}{\partial t}. \end{aligned} \tag{8}$$

Eq. (8) has two breakthroughs: (1) the new first and second equations are linked, describing electric and magnetic fields respectively, and (2) the absence of conduction current leads to symmetry in the third and fourth equations. Based on the first and second of Eq. (8), a crystal composed of electron-proton (ion) pairs can be viewed as a super large-scale integrated capacitor. The current is interpreted as an electromagnetic wave with the third and fourth equations. As a result, research on avoiding collisions between electrons and the lattice in superconductivity has been transformed into an investigation into reducing the loss of electromagnetic waves during propagation within wires.

C. Mott insulator and order parameters

The above research has shown that the energy gap symmetry is not the key to superconductivity, but the key to the superconductivity mechanism is the localization of electrons. For the convenience of discussion, we ignore the influence of negatively charged ions on the energy gap symmetry around the localized electrons. In that case, both conventional and unconventional superconductors can be simplified to the quasi-two-dimensional Mott crystal structure in Fig. 10(a), and the green contour line represents the Coulomb field of the ions in the nearest adjacent layers. Under this assumption, we can establish a unified superconducting theory suitable superconductors. When Fig. 10(a) is

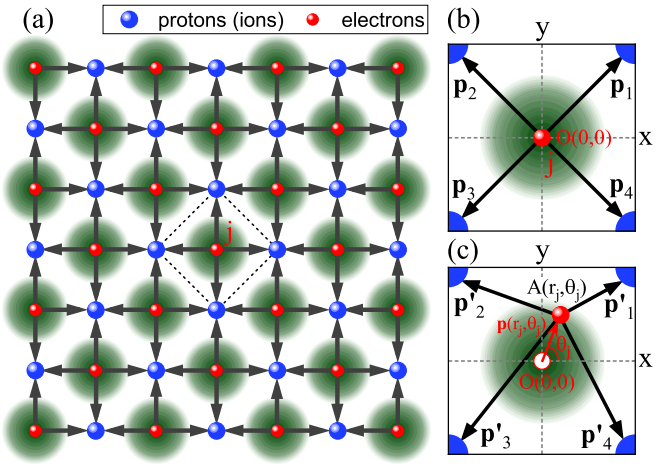

FIG. 10. (a) The electric dipole vector represents 2D Mott insulator with the intrinsic antiferromagnetic long-range order, (b) a electron in ground state; (c) the electron in excited state.

decorated with the electric dipole vectors, showing the inherent antiferromagnetic long-range order. If capacitors represent the electron-proton pairs, the total capacitance of the Mott insulator is zero due to symmetry. Therefore, it appears as an insulator that cannot conduct electricity.

Fig. 10(b) is the unit cell, where four degenerate electric dipole vectors ($\mathbf{p}_1$, $\mathbf{p}_2$, $\mathbf{p}_3$, and $\mathbf{p}_4$) can be integrated into a total vector $\mathbf{P}_{\rm O}= 0$. As shown in Fig. 10(c), external factors (temperature, pressure, and electromagnetic fields) can cause the ground state electron to enter an excited state $A(r_j, \theta_j)$ with a vector $\mathbf{p}(r_j, \theta_j) = e\mathbf{r}_{\rm j}$. The sum of four electric dipole vectors ($\mathbf{p'}_1$, $\mathbf{p'}_2$, $\mathbf{p'}_3$, and $\mathbf{p'}_4$) is expressed as $\mathbf{P}_{\rm A} = -\mathbf{p}(r_j, \theta_j) = -er_j \exp(i\theta_j)$. The emergence of the vector $\mathbf{P}_A$ indicates the excitation of a hidden magnetic state in the superconducting parent, leading to the destruction of the Mott antiferromagnetic phase. Moreover, the vector can function as the spin and magnetic moment of the excited electrons. Notably, the Electron's magnetism or spin arises from a combination with positively charged lattices, disappearing upon departing material and becoming free. Electrons do not have intrinsic spin, explaining the observed charge-spin separation in experiments [31].

The Ginzburg-Landau theory is the most successful theory of superconductivity, capturing the order parameter and symmetry breaking of superconducting phase transition. However, it cannot address the microscopic question of what constitutes the order parameter with electromagnetic properties. Our theory can answer this question. For a conductor with N valence electrons, by using $\mathbf{P}_A$, the complex order parameter can be defined as:

$$\mathbf{P}_{order} = \frac{e}{N}\sum_{j=1}^{N} r_j \exp(i\theta_j). \tag{9}$$

Using Eq. (9), it is possible to distinguish among the typical condensed states and display their essential differences at the microscopic scale.

V. ZERO RESISTANCE AND MEISSNER EFFECT

The zero electrical resistance exhibited by superconductors in the presence of an applied electric field and the manifestation of the Meissner effect in the presence of a magnetic field are two crucial criteria for determining superconductivity. However, at the microscopic level, the changes in superconducting electrons inside the material before and after the phase transition still need to be fully understood. This lack of understanding is why research in superconductivity theory has become stuck. In the following, we aim to unveil the microscopic origins of these two key superconducting phenomena.

A. The Essence of Zero Resistance in Superconductivity

In order to interpret the cause of zero resistance more intuitively, Fig. 10(a) can be further simplified as the

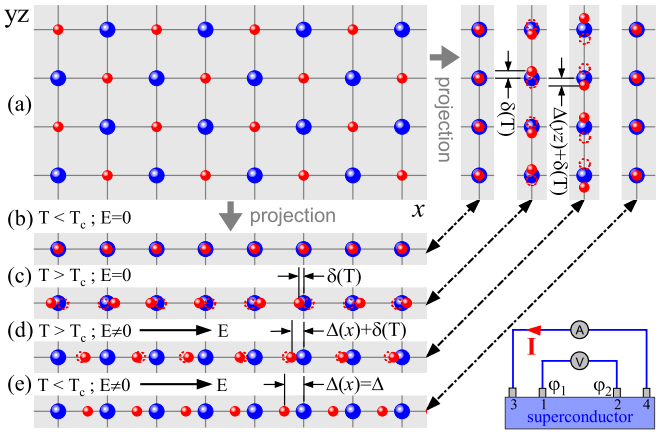

FIG. 11. Four condensed states based on symmetry and symmetry breaking: (a) insulating state; (b) the projection of (a) exhibiting a perfect symmetry; (c) normal state under random thermal motion; (d) when $T > T_c$, metallic state driven by the electric field; (e) when $T < T_c$, the superconductor entering a completely symmetrical broken superconducting state, where all electrons have the same displacement in the opposite direction of the electric field. The insulated state (a) serves as the preparatory state for the superconducting state (e). Gold, silver, and copper are good conductors but not superconductors, as the low-temperature technology fails to induce their insulated state.

superconducting surface of Fig. 11(a). Under the condition of no external electromagnetic field and $T < T_c$, the electron is in the ground state without symmetry breaking, which can be clearly shown in the projection Fig. 11(b). At this time, the order parameter $\mathbf{P}_{order}$ and the total capacitance of the superconductor are all zero, and the superconductor behaves as an antiferromagnetic insulator. Therefore, as a necessary condition, the ground state of any superconductor must be a Mott insulator. For good conductors such as Au, Ag, and Cu, because valence electrons are very active, they cannot condense into the insulating state at the lowest temperature that can be realized in the lab, so they do not exhibit superconductivity. When measuring Fig. 11(a) or Fig. 11(b) using the four-wire method, the potentials (φ_1) and (φ_2) on the superconducting surface induced by voltage electrodes 1 and 2 are both zero due to the cancellation of potentials generated by positive and negative charges inside the superconductor.

The second scenario depicted in Fig. 11(c) is the normal state, when $T > T_c$, the electrons absorb random thermal energy and then leave their equilibrium position with random displacement δ(T). Since random thermal motion does not destroy the overall symmetry, the superconductors' average order parameters and total capacitance remain zero.

Fig. 11(d) represents the metallic state. Assuming an external electric field is applied along the x-direction, when $T > T_c$, due to the combined effect of electric field and random thermal motion, electrons undergo displacements Δ(x) + δ(T) and Δ(yz) + δ(T) in the directions parallel and perpendicular to the electric field. As a result of thermal motion, the electromagnetic field energy does not

propagate strictly along the x-direction but experiences losses along the yz-direction. In other words, as the propagation distance x increases, the electromagnetic field energy (or current) gradually attenuates, and the attenuated electromagnetic energy is manifested as losses in the zy-direction, contributing to the resistance. In this scenario, the potentials $\varphi_1 > \varphi_2 \neq 0$, resulting in a voltage between the two electrodes, $\mathrm{V} = \varphi_1 - \varphi_2 \neq 0$ and the resistance $\mathrm{R} = \mathrm{V/I} \neq 0$.

Fig. 11(e) illustrates the superconducting state in which thermal disturbance is wholly suppressed. This state arises from a Pierce-like dimerization pairing transition that leads to perfect symmetry breaking along the direction of the applied electric field, while no symmetry breaking occurs in the vertical yz-direction. Since the electric field energy (current) does not decay, the displacement $\Delta(\mathrm{x}) = \Delta$ of the electrons is the same for all. As a result, the order parameter of Eq. (9) describing the superconducting phase transition reaches its maximum value $\mathbf{P}_{order} = e\Delta$. This means that all electrons undergo coherent condensation and enter the superconducting state. Because Δ is a constant quantity, therefore $\varphi_1 = \varphi_2 \neq 0$ and $\mathrm{V} = \varphi_1 - \varphi_2 = 0$; consequently, the resistance $\mathrm{R} = \mathrm{V/I}$ becomes zero, indicating zero resistance in the experiments.

In the new paradigm, the essence of electric current is the energy of the input electromagnetic field. The main difference between the metallic state and the superconducting state lies in the presence or absence of energy loss during the transmission of electromagnetic energy. In the case of the superconducting state, electrons undergo a symmetric breaking along the electric field direction, forming an array of capacitors. This opens up a lossless pathway for the propagation of electromagnetic energy. On the other hand, in the metallic state, the capacitive pathway in the direction perpendicular to the electric field is also opened, leading to leakage of electromagnetic field energy and the formation of resistance. Suppose the valence electrons are severely bound and cannot undergo a symmetrical breaking phase change under the influence of an external field. In that case, the capacitor path will remain closed, and the material will remain in a non-conductive insulation state. Because electrons are no longer the carriers of electric energy, the transmission of current does not need the long-distance movement of electrons in the lattice. The problem of avoiding the collision between moving electrons and lattice in superconducting research, which has long plagued the physics community, does not exist.

B. Meissner effect puzzle

Besides exhibiting zero resistivity, superconductors are also characterized by impeccable diamagnetism, referred to as the Meissner effect. It is conventionally believed that superconductors placed in a weak external magnetic field $\mathbf{H}$ will expel the magnetic field from their interior upon cooling to below their transition temperature. The magnetic field expelled picture of Fig. 12 shows that the Meissner effect

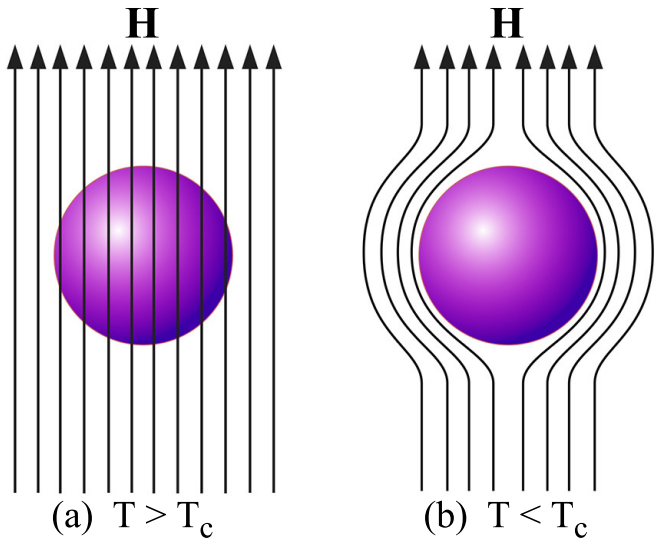

FIG. 12. The mainstream explanation of the Meissner effect: (a) above the critical temperature, the magnetic field is able to penetrate the superconductor, (b) below the critical temperature, the magnetic field is excluded from the interior of the superconductor.

is a time-dependent dynamic process. Hence, any valuable theory of superconductivity must be able to explain how the superconductor goes from the normal to the superconducting state by expelling the magnetic field against Faraday's law. In this study, we aim to solve this puzzle by only employing the microscopic mechanism of proton-electron electric dipole pairing.

Figs. 13(a) and (b) demonstrate repulsion and attraction

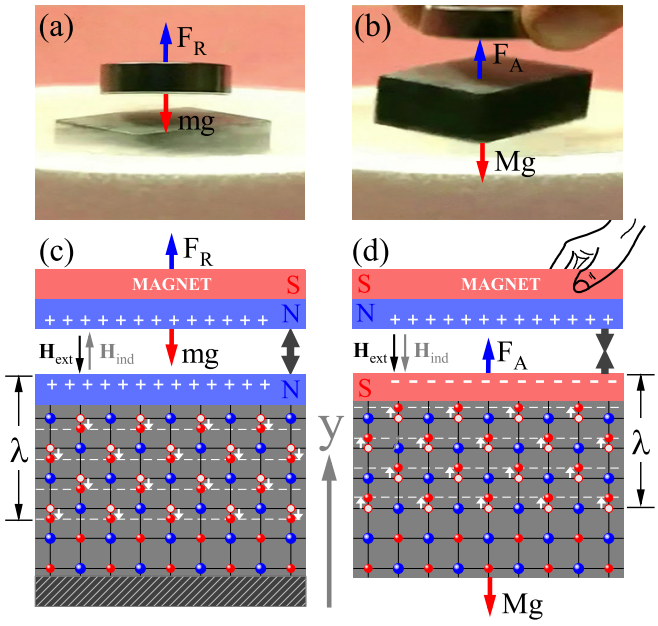

FIG. 13. The Meissner experiment and new explanation: (a) and (b) observed repulsion and attraction interactions; (c) and (d) corresponding theoretical explanations of confined electrons.

between the superconductor and magnet, with the repulsion or attraction rapidly switching. Assuming the masses of the magnet and superconductor are m and M, respectively, the repulsive and attractive forces satisfy the force balance: $F_R = mg$ and $F_A = Mg$, where g is the acceleration of gravity.

In our theory, as shown in Fig. 13(c), a magnet $\mathbf{H}_{\rm ext}$ above a superconductor causes the magnet to fall due to the gravitational field, increasing the strength of the magnetic field within the superconductor. This generates an induced magnetic field $\mathbf{H}_{\rm ind}$ in the opposite direction and a repulsive interaction between the magnet and the superconductor due to the same sign of charges on adjacent surfaces. Fig. 13(d) shows that lifting the magnet away causes a decrease in magnetic field strength within the superconductor, generating an induced magnetic field $\mathbf{H}_{\rm ind}$ in the same direction as, leading to mutual attraction between the magnet and superconductor due to the net charge on their nearest neighboring surfaces being of different signs. In the figure, λ is the London penetration depth, which automatically adjusts according to external factors such as the mass of magnets and superconductors to achieve force balance.

VI. CONCLUDING REMARKS

In conclusion, we have established a theoretical framework centered around polyhedron quantum-well-confined electrons, building upon experimental evidence from angle-resolved photoemission spectroscopy (ARPES) and neutron scattering in high-temperature copper-based and iron-based superconductors. This research represents a groundbreaking and innovative approach, replacing the dynamic paradigm of free electrons with a static paradigm based on localized electrons. By incorporating four well-established scientific hypotheses, namely the Mott insulator, Maxwell's displacement current, the Dirac magnetic monopole, and the Ginzburg-Landau symmetry-breaking theory, we have successfully developed a unified superconducting theory applicable to both conventional and unconventional superconductors.

This new theory merges electric and magnetic fields, revealing the intrinsic connection between magnetism and superconductivity while achieving the symmetry of Maxwell's equations. Within this unified theoretical framework, we have effectively explained numerous fundamental phenomena observed in high-temperature superconductors and condensed physical phase transitions. It enables the analytical determination of critical properties in copper-based and iron-based superconductors, such as the structure of the Fermi surface, the value and symmetry of the superconducting energy gap, the superconducting transition temperature, and the spin resonance peak parity. Remarkably, the predictions of our theory align well with experimental findings. Moreover, our research offers fresh insights into the microscopic nature of the Ginzburg-Landau order parameter, the phenomenon of zero resistance, and the Messner effect. We propose that the proton-electron pairing mechanism holds the potential to shed new light on various physical phenomena.

In recent decades, it is an undeniable fact that physics research has stagnated. In our opinion, the main reason for this situation is that researchers have unquestioningly created a plethora of physical concepts, mainly attributing excessive mystical powers to electrons, such as spin, quantum entanglement, Pauli exclusion principle, persistent current, emission and absorption of photons, Cooper pairing, and so on. When playing with concepts and creating models becomes fashionable, it becomes a dead-end for physics research. It is impossible for any motion in nature to be eternal, and electron motion inevitably involves energy loss, and collective electron motion necessarily exhibits dispersion and diffusion. These are objectively determined facts based on the laws of thermodynamics. Clearly, the dynamic image of electrons cannot generate coherent condensation and superconductivity. As suggested in this paper, the static state, where energy is minimized, is the only state that can achieve coherent condensation in superconductivity. From the research of this paper, the physics community should realize that we can only envision a promising future by grounding physics research in experimental facts.

ACKNOWLEDGMENTS

The author would like to acknowledge Prof. Duan Feng for his invaluable suggestions and helpful discussions at the early stage of this research. The author would also like to express his appreciation to Prof. Changde Gong for the opportunity to comprehend the fascinating world of superconductivity. Special thanks go to Prof. Dingyu Xing for his supportive and considerate care of the author's personal and family. Finally, the author extends his deepest gratitude to Prof. Shusheng Jiang for his unwavering encouragement, support of the research process, and provision of living arrangements and research resources.

[1] H. K. Onnes, Leiden Comm. **119b**, 122 (1911).
[2] J. Bardeen, L. N. Cooper and J. R. Schrieffer, Phys. Rev. **106**, 162 (1957).
[3] J. G. Bednorz and K. A. Muller, Z. Phys. B. **64**, 189 (1986).
[4] M. K. Wu, et al., Phys. Rev. Lett. **58**, 908 (1987) .
[5] C. W. Chu, et al., Phys. Rev. Lett. **58**, 405 (1987).
[6] H. Maeda, et al., Jpn. J. Applk. Phys. **27**, L209 (1988).
[7] Y. Kamihara, T. Watanabe, M. Hirano, and H. Hosono, J. Am. Chem. Soc. **130**, 3296 (2008).
[8] X. H. Chen, et al., Nature **453**, 761 (2008).
[9] Z. A. Ren, et al., Chin. Phys. Lett. **25,** 2215 (2008).
[10] P. W. Anderson, Science **235**, 1196 (1987).
[11] C. J. Halboth and W. Metzner, Phys. Rev. Lett. **85**, 5162 (2000).
[12] G. Baskaran and P. W. Anderson, Phys. Rev. B **37**, 580 (1988).

[13] F. C. Zhang and T. M. Rice, Phys. Rev. B **37**, 3759 (1988).
[14] D. J. Scalapino, E. Loh, Jr., and J. E. Hirsch, Phys. Rev. B **34**, 8190 (1986).
[15] A. Damascelli, Z. Hussain, and Z. X. Shen, Rev. Mod. Phys. **75**, 473 (2003).
[16] J. M. Tranquada, et al., Nature **375**, 561 (1995).
[17] P. W. Anderson, Science **317**, 1705 (2007).
[18] T. Valla, et al., Science **285**, 2110 (1999).
[19] K. M. Shen, et al., Science **307**, 901 (2005).
[20] H.-B. Yang, et al., Nature **456**, 77 (2008).
[21] P. Ai, et al., Chin. Phys. Lett. **36**, 067402 (2019).
[22] A. A. Kordyuk, Low Temp. Phys. **38**, 888 (2012).
[23] H. Ding, et al., EPL **83**, 47001 (2008).
[24] Y. Zhang, et al., Nature Materials **10**, 273 (2011).
[25] L. Gao, et al., Phys. Rev. B **50**, 4260 (1994).
[26] L. Sun, et al., Nature **483**, 67 (2012).
[27] F. F. Tafti, et al., Nature Physics **9**, 349 (2013).
[28] D. S. Wu, et al., Phys. Rev. B **101**, 224508 (2020).
[29] T. Xie, et al., Phys. Rev. Lett. **120**, 267003 (2018).
[30] D. F. Liu, Nature Communications **3**, 931 (2012).
[31] C. Kim, et al., Phys. Rev. Lett. **77**, 4054 (1996).
[32] V. L. Ginzburg and L. D. Landau, Zh. Eksp. Teor. Fiz. **20**, 1064 (1950).
[33] P. A. M. Dirac, Proc. Roy. Soc. **A 133**, 60 (1931).
[34] G. E. Uhlenbeck and S. Goudsmit, Nature, **117**, 264 (1926).